SURFACE ENGINEERING OF TITANIUM VIA MICRO-ARC OXIDATION WITH HYDROXYAPATITE/NANO-SILVER COMPOSITE COATINGS: IN VITRO AND IN VIVO BIOLOGICAL PERFORMANCE EVALUATION

UDC:669.295:615.46
Original scientific paper https://doi.org/10.46793/adeletters.2025.4.3.4

Nabaa S. Radhi[1], Saja Hamzah[2], Talib Abdulameer Jasim[3], Zainab Al-Khafaji[4,5*], Mayadah Falah[6], Waleed Muwafaq Al-Aloosi[7]

[1]Metallic Engineering Department, College of Materials Engineering, University of Babylon, Babylon, Iraq
[2]Babylon Governorate Court, Iraq
[3]Department of Aeronautical Technical Engineering, College of Technical Engineering, Al-Farahidi University, Baghdad, Iraq
[4]Scientific Research Center, Al-Ayen University, Thi-Qar, 64001, Iraq
[5]Department of Civil Engineering, Faculty of Engineering and Built Environment, Universiti Kebangsaan Malaysia, 43600 UKM Bangi, Selangor, Malaysia
[6]Building and Construction Techniques Engineering Department, College of Engineering and Engineering Techniques, Al-Mustaqbal University, 51001, Babylon, Iraq
[7]Department of Medical Instruments Engineering Techniques, College of Engineering, University of Al Maarif, Al Anbar, 31001, Iraq

Abstract:
Titanium (Ti) implants often suffer from limited bioactivity and corrosion susceptibility, necessitating advanced surface modifications to enhance their clinical performance. In this study, hydroxyapatite (HA) and HA/nano-silver (HA/nAg) composite coatings were fabricated on Ti substrates using the micro-arc oxidation (MAO) method at 200 V with deposition times of 30–60 s and Ag loadings of 0.5–2 g/L. Experimental evaluations demonstrated that HA/nAg coatings exhibited markedly improved surface roughness, hardness, and corrosion resistance compared to uncoated Ti. Vickers hardness increased significantly with the incorporation of 0.5–1 g/L Ag, reaching a maximum of 162.25 HV, whereas higher Ag concentrations (>1.5 g/L) caused a decline due to microstructural defects. Antibacterial testing revealed effective inhibition of *E. coli* growth for all Ag-containing coatings, with enhanced osseointegration confirmed in vivo by histology and quantitative metrics. Histomorphometric analysis showed that 1 g/L Ag achieved the highest bone–implant contact (65.2%) and bone volume density (51.5%), outperforming both uncoated Ti and pure HA coatings. Conversely, excessive Ag loadings were associated with reduced BIC and BV/TV, reflecting silver-induced cytotoxicity. Collectively, these findings identify HA/nAg coatings, particularly at 1 g/L Ag and 60 s deposition, as the optimal condition for enhancing corrosion resistance, antibacterial activity, and osseointegration of titanium implants.

ARTICLE HISTORY
Received: 4 August 2025
Revised: 15 September 2025
Accepted: 24 September 2025
Published: 30 September 2025

KEYWORDS
Tissues, Micro-Arc Oxidation, Surgical Process, Titanium alloys, coatings

1. INTRODUCTION

Titanium (Ti) and its alloys have been extensively employed in biomedical applications since the mid-20th century owing to their high specific strength, low density, excellent corrosion resistance, and outstanding biocompatibility, making them suitable for orthopedic, maxillofacial, and dental implants [1–6]. Despite these advantages, the intrinsic bio-inertness of Ti surfaces

*CONTACT: Zainab Al-Khafaji, e-mail: P123005@siswa.ukm.edu.my

limits their ability to stimulate osteoblastic differentiation and proliferation, often resulting in delayed osseointegration and an increased risk of implant-associated complications such as bacterial colonization and biofilm formation [7–10]. Such limitations can compromise implant longevity and lead to aseptic loosening or infection-driven failure, highlighting the need for advanced surface modification strategies that enhance both osteoconductivity and antibacterial performance [11].

Surface characteristics – chemical composition, specifically topography, hydrophilicity, and roughness – play a decisive role in the host tissue response, influencing protein adsorption, cell adhesion, and subsequent bone remodeling [11,12]. Various mechanical (e.g., sandblasting, grinding), physical (e.g., ion implantation, physical vapor deposition), and chemical (e.g., sol–gel processing, chemical vapor deposition, anodization) modification methods have been explored to improve the bioactivity of Ti and its alloys [13–15]. Among these, MAO, also known as plasma electrolytic oxidation, has emerged as a promising approach for biomedical applications due to its ability to produce thick, adherent, and porous ceramic oxide layers directly on valve metals under high-voltage conditions [16,17]. These MAO-derived coatings exhibit superior wear and corrosion resistance, enhanced bioactivity, and strong mechanical interlocking with bone tissue [15,18,19]. However, conventional MAO surfaces may present micro-pores and micro-cracks, which can serve as bacterial entry points and compromise long-term stability if not functionally optimized [16].

MAO entails plasma discharge; yet, it is distinct from conventional plasma electrolytic discharge methods such as plasma cutting or welding. It is frequently confused with anodic oxidation (AO). However, they are distinct processes and technologies. MAO often necessitates higher voltage and reduced processing durations, with the electrolyte type and the properties of the resultant coating markedly differing from those of AO. Currently, the majority of academics categorise the MAO process into three types: arc discharge, micro-arc discharge, and spark discharge. Some include the first brief anodising process, resulting in a total of 4 phases. The process of MAO coating development is fundamentally consistent, irrespective of the electrolytes or control method utilised [20].

Hydroxyapatite (HA), a calcium phosphate ceramic chemically analogous to the mineral phase of bone, has been extensively incorporated into Ti-based coatings to enhance osseointegration and bioactivity [21–24]. Nevertheless, HA lacks inherent antibacterial capability, leaving implants susceptible to peri-implant infections [25]. The incorporation of silver nanoparticles (nAg) into HA matrices offers a dual-functionality approach: HA promotes bone bonding and mineralization, while nAg provides broad-spectrum antibacterial activity through mechanisms such as disruption of bacterial cell membranes, generation of reactive oxygen species, and interference with microbial metabolic pathways [26–28].

The functional performance of hydroxyapatite/nanosilver (HA/nAg) composite coatings is strongly governed by the silver content, the degree of nanoparticle dispersion, and the resulting coating microstructure. Controlled silver ion release at moderate levels has been shown to enhance antibacterial activity; however, excessive concentrations may induce cytotoxicity and hinder tissue regeneration [29]. Achieving an optimal balance requires rigorous control of key deposition parameters, including nanosilver loading and coating duration, to simultaneously ensure antibacterial efficacy, biocompatibility, and mechanical integrity [30]. Moreover, comprehensive in vivo investigations are indispensable to establish whether the favorable in vitro outcomes can be reliably translated into effective osseointegration and sustained clinical performance [31].

In alignment with prior investigations, the present study adopted silver addition ratios within the reported safe thresholds. The incorporation level did not exceed 2 wt.% Ag, as higher concentrations have been shown to exert cytotoxic effects on host tissues, leading to the destruction of living cells rather than selectively inhibiting bacterial proliferation. In this context, the present study aims to develop and optimize HA/nAg composite coatings on Ti substrates via the MAO technique, systematically evaluating the effects of silver nanoparticle concentration (0.5–2 g/L) and coating duration (30–60 s) on structural morphology, surface roughness, microhardness, corrosion resistance, antibacterial performance, and osseointegration in a rabbit femoral implantation model. The findings of this work are expected to contribute to the development of bioactive, infection-resistant Ti-based implants with

enhanced long-term reliability in load-bearing biomedical applications.

2. MATERIALS AND METHODS

2.1 Micro Arc Oxidation (MAO)

Micro-arc oxidation (MAO) is an advanced electrochemical surface modification technique capable of producing thick, adherent, and functionally graded oxide layers on valve metals such as titanium, magnesium, and aluminum alloys, as well as on ceramic substrates, in a single processing step [30]. The process is conducted at applied voltages exceeding the dielectric breakdown threshold of the electrolyte–metal interface, inducing localized plasma discharges that generate a transient oxygen gas sheath around the anode. These discharges manifest as intense luminous micro-arcs, as illustrated in Figs. 1 and 2, and facilitate the simultaneous incorporation of electrolyte-derived species into the growing oxide matrix [31].

In this study, commercially pure titanium (CP-Ti) plates with a nominal purity of 99.7% and a thickness of 0.1 mm were precision-sectioned into 1 × 1 cm specimens. Prior to coating, all substrates underwent ultrasonic cleaning in analytical-grade ethanol for 10 minutes to remove organic contaminants and promote coating adhesion. The MAO electrolyte was prepared as an aqueous solution containing 0.06 mol/L sodium biphosphate dihydrate ($NaH_2PO_4 \cdot 2H_2O$) and 0.13 mol/L calcium acetate monohydrate ($(CH_3COO)_2 \cdot Ca \cdot H_2O$), adjusted to a pH of 2.3 using hydrochloric acid.

To fabricate bioactive and antibacterial composite coatings, nanosilver (nAg) particles were introduced into the hydroxyapatite-based electrolyte at controlled concentrations of 0, 0.5, 1.0, 1.5, and 2.0 g/L. This systematic variation enabled the evaluation of silver loading effects on coating microstructure, phase composition, and functional properties.

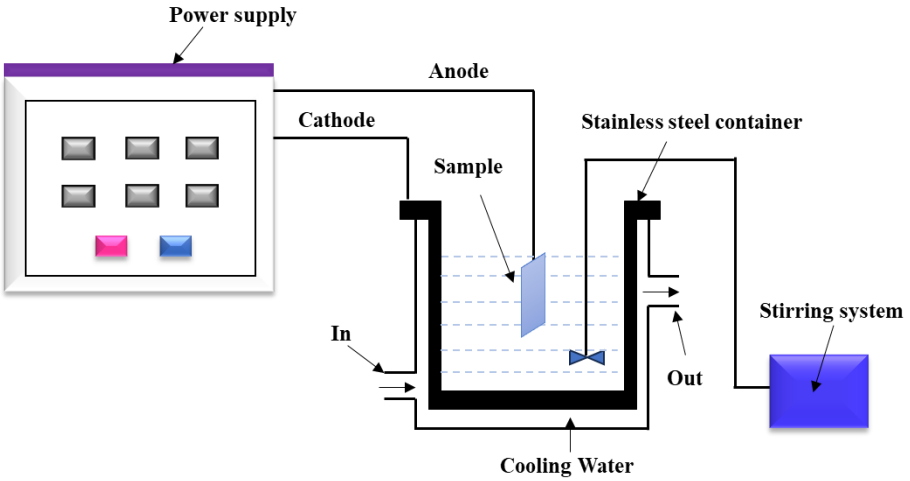

Fig. 1. Graphic representation of the MAO setup process

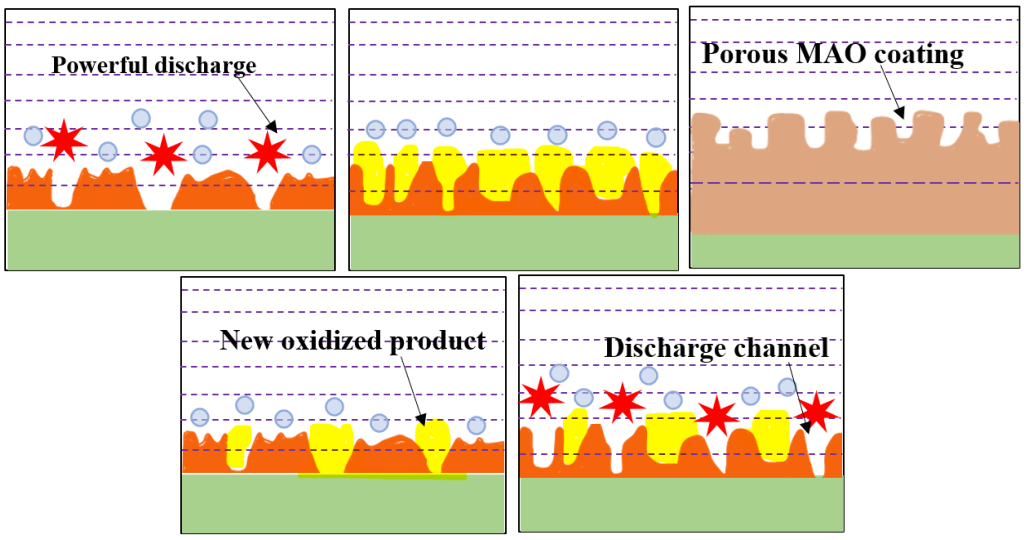

Fig. 2. Graphic representation (MAO) working mechanism in the porous coating

In the preliminary experimental trials, coating was attempted at applied voltages of 100, 200, and 300 V; however, the deposited layers were discontinuous and exhibited pronounced cracking across various deposition times (15, 30, 45, and 60 s). Subsequent optimization revealed that the most stable and uniform coating parameters were established and validated in the practical experimental section. Table 1 explores the required variables for completing the coating (HA/nAg, HA) on a Ti-plate, which includes a constant voltage of 200 V, durations of 30, 45, or 60 s, and the weight % of nano silver.

Table 1. Various factors of the coating process

Sample ID	Sample	Duration (s)	Ratio of adding nAg (g/L)
A	Ti	-	-
B	HA	30	0
C	HA	45	0
D	HA	60	0
E	HA/ Ag	30	0.5
F	HA/ Ag	45	0.5
G	HA/ Ag	60	0.5
H	HA/ Ag	30	1
I	HA/ Ag	45	1
J	HA/ Ag	60	1
K	HA/ Ag	30	1.5
L	HA/ Ag	45	1.5
M	HA/Ag	60	1.5
N	HA/ Ag	30	2
O	HA/ Ag	60	2

2.2 Tests

Tests were conducted to assess the performance of composite coating layers (HA, HA/nAg) on specimens in this study, which can be classified into in vitro and in vivo tests:

2.2.1 Energy Dispersive X-ray Spectroscopy (EDS)

Energy Dispersive X-ray Spectroscopy (EDS) was employed to identify and quantify the elemental composition of the specimens. Samples were polished, ultrasonically cleaned, and carbon-coated to minimize charging. Analyses were performed in a field-emission SEM equipped with a silicon drift detector at 15 kV accelerating voltage, 10 mm working distance, and 60–120 s live time.

2.2.2 Coating Thickness Test

For determining the HA and HA-nAg layer thickness, the thickness measurement apparatus known as the D-5870 HEMER-Sundwing, located in West Germany, was utilized.

2.2.3 Atomic Force Microscopy Test

In the past, this test has been utilized to observe and analyze surface structure with a resolution and precision that had never been seen before. For instance, pictures (images) demonstrating the organization of individual atoms in a sample can be obtained using an atomic force microscope (AFM, contact mode, SPM AA3000 Angstrom Advanced Inc., USA). Furthermore, the structure of individual molecules of an HA/nAg composite coating can be visualized.

Topographical imaging alone often fails to provide the necessary insights for researchers, and the surface topology frequently does not correspond to the material characteristics. Consequently, improved imaging modalities were created to provide quantitative data on diverse surfaces. Currently, several material characteristics may be assessed using AFM methods, including resistance, surface potential, viscoelasticity, conductivity, magnetic forces, capacitance, electrical forces, and friction.

2.2.4 Surface Roughness Test

Utilizing the roughness measurement instrument (HSR210) allowed for the surface of the composite coating (HA, HA/nAg) that was applied to the Ti-substrate to be evaluated for its level of roughness. The roughness that is present on the surface may be characterized as an irregularity in the profile of the surface.

2.2.5 Fields Emission Scanning Electron Microscopy (FESEM)

Field emission scanning electron microscopy (FESEM) was employed to examine the porosity, crack propagation, morphological features, and overall homogeneity of the coating. This advanced imaging technique provides detailed topographical and compositional information at magnifications up to 25,000×, while offering an exceptionally high depth of field. In contrast to conventional scanning electron microscopy (SEM), FESEM produces images of superior clarity with minimal electrostatic

distortion, achieving spatial resolutions approaching 1.5 nm—representing a three- to six-fold improvement over traditional SEM.

2.2.6 Microhardness Test

Vickers Hardness (TH-717 Digital Micro Vickers Hardness Tester) has been utilized to measure the hardness of the HA and HA-nAg layer at load (100 N) and a holding duration of 15 s, according to ASTM E384-22.

2.2.7 Corrosion Rate Measurements Test

One straightforward way to determine the corrosion rate of a metal involves submerging specimens in a test medium (such as Ringer's solution) and tracking the decrease in weight of the material over time. Calculating the loss between the initial and final values helps determine the corrosion rate (CR) utilizing the provided Eq. 1 [32]:

$$CR = \frac{W_o - W_i}{A \cdot t}, \quad (1)$$

where are:
CR - is corrosion rates (mpy),
Wo - is the original weight (g),
Wi - is the weight after immersion (g),
i - express the number of days,
A - is an area of the sample (cm^2),
t - is duration in days.

2.2.8 Antibacterial Test

When biomaterials, particularly metallic implants, are implanted in the human body, they come into contact with bacteria, leading to infections in the surrounding cells near the implant. Hence, it is crucial to determine the presence of bacteria on Ti-substrate and composite coating (HA, HA/nAg) specimens through antibacterial testing. The experiment involved washing the specimen in a Petri dish with mannitol salt agar and leaving it in the dish for 5 minutes. The mixture was then separated into 0.5 ml portions and transferred to another petri dish for incubation at 37 degrees Celsius for one day.

2.2.9 Surgical Procedure and Implantation Test

Six skeletally mature male rabbits of local origin, each with a body mass ranging from 2 to 3 kg, were selected as the in vivo model for the osseointegration assessment. Animals were housed in standard stainless-steel cages under controlled environmental conditions, with ad libitum access to tap water and a balanced diet comprising commercially available pellets supplemented with fresh vegetables. To ensure physiological acclimatization, all subjects were maintained in identical housing conditions for a three-day preoperative period.

All surgical instruments and implant specimens were sterilized according to standard protocols prior to the procedure. General anesthesia was induced by intramuscular injection of xylazine and ketamine at clinically appropriate dosages to provide adequate sedation and analgesia. Surgery was performed under aseptic conditions in a controlled operating environment. The left hind limb of each rabbit was shaved with a sterile razor and prepared with 70% ethanol, followed by povidone–iodine, after which the site was draped with sterile surgical cloths.

A longitudinal skin incision of approximately 3.5 cm was made to expose the femoral diaphysis. The fascia and surrounding soft tissues were carefully retracted to reveal the periosteum. As shown in Fig. 3(a–b), a cylindrical cavity was drilled using a 2 mm bit with intermittent pressure to minimize thermal damage. The cavity was subsequently enlarged to match the dimensions of the implant. Cylindrical implants, each 5 mm in length, were then inserted into the prepared sites with light press-fit, ensuring complete seating and intimate contact with the host bone tissue (Fig. 3(c–d)).

Following implantation, the fascia was approximated using absorbable Suteon sutures, and the skin was closed with interrupted sutures, as depicted in Fig. 3(e). Postoperative care included intramuscular administration of a broad-spectrum antibiotic and a nonsteroidal anti-inflammatory drug (Voltaren) for three consecutive days to prevent infection and manage postoperative inflammation.

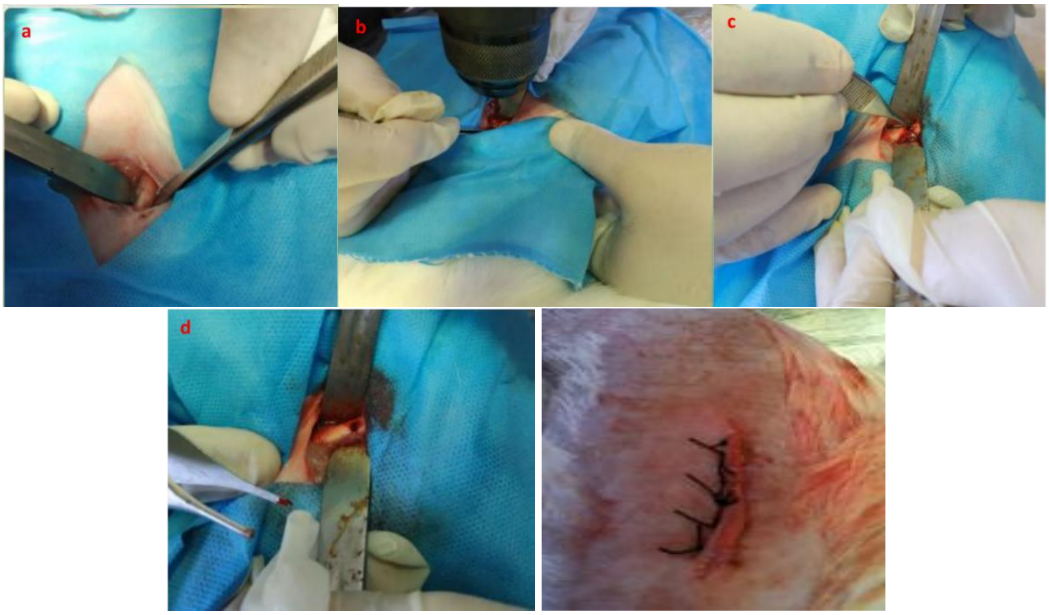

Fig. 3. The surgery process: a) surgical clamps and towels, a reflection of skin and reflection fascia and muscles; b) preparation of holes; c) The hole; d) Insert the implants; and e) Stitching of skin

2.2.10 Histological Testing

Bone sectioning was performed after the euthanasia of the animal by an overdose of general anesthesia at 40-day intervals. An optical microscope has been used to analyze the histology of the implant. A cutting tool was used to get a bone-implant block. The bone-implant block was immersed in 10% freshly prepared formalin and maintained for a duration of 3 weeks.

The histology specimen was preserved in 10% formalin for two days at room temperature and then rinsed with tap water for two hours. The sample was then decalcified using the formic acid-sodium citrate method. Upon completion of decalcification, the sample was rinsed with tap water for four hours [33,34]. The sample was processed utilizing standard histological techniques involving mounting, sectioning, embedding, infiltration, clearing, dehydration, staining with Hematoxylin and eosin (H&E), and cover slipping and labeling [33].

Utilizing a series of alcohol concentrations starting from 50% and increasing to 100%, dehydrate for 2 hours at each concentration. Rinse with Xylen twice for 10-50 minutes each time. Immerse the tissue specimens in paraffin wax at 56.5-58°C overnight. Encasing the samples in paraffin wax to create blocks and slicing the samples into thin sections of 5-7µm with a rotary microtome. Rehydration involves a sequence starting with 100, 90, 80, 70, 60, and 50% alcohol. After staining the samples with Mayer's H&E and Masson's trichrome stains and mounting, the process involved adding DPX and placing a cover slide on the section strip on glass slides to cover it [35]. Eventually, analyze the histological slides utilizing a light microscope.

2.2.11 Bone–Implant Contact (BIC%) and Bone Volume Density (BV/TV%)

Bone–implant contact (BIC%) and bone volume density (BV/TV%) were quantified from undecalcified histological sections using calibrated image analysis (ImageJ). BIC% was calculated as the ratio of bone directly contacting the implant surface to its total perimeter, whereas BV/TV% represented peri-implant mineralized bone fraction.

$$\mathrm{BIC}(\%) = \frac{L_{\mathrm{BIC}}}{L_{\mathrm{peri}}} \times 100, \tag{2}$$

$$\frac{\mathrm{BV}}{\mathrm{TV}(\%)} = \frac{V_{\mathrm{bone}}}{V_{\mathrm{tissue}}} \cdot 100, \tag{3}$$

where are:

L_{BIC} - cumulative length of bone-in-contact along the same perimeter (µm),

L_{peri} - total traced implant perimeter within ROI (µm),

V_{bone} - refers to bone volume (mm³),

V_{tissue} - refers to total tissue volume (mm³).

3. RESULTS AND DISCUSSION

3.1 EDX Analysis

The Energy Dispersive X-ray Spectroscopy (EDS) results shown in Fig. 4 confirm the successful surface modification of commercially pure titanium

(CP-Ti) with hydroxyapatite and HA/nAg composite coatings. In the spectrum of uncoated titanium (a), strong Ti peaks are observed together with a minor oxygen signal, corresponding to the spontaneous formation of a thin TiO_2 layer. After deposition of hydroxyapatite (b), distinct calcium and phosphorus peaks appear alongside oxygen, consistent with the presence of the HA phase. The measured Ca/P ratio closely matches the stoichiometric composition of $Ca_{10}(PO_4)_6(OH)_2$, verifying the formation of a bioactive coating layer. In the case of the HA/nAg composite coating (c), additional silver peaks (Ag Lα, Ag Lβ) are distinctly observed alongside Ca, P, and O signals, signifying the effective integration of Ag nanoparticles within the HA matrix. The attenuation of Ti peak intensity in both coated samples reflect the shielding effect imparted by the deposited layers.

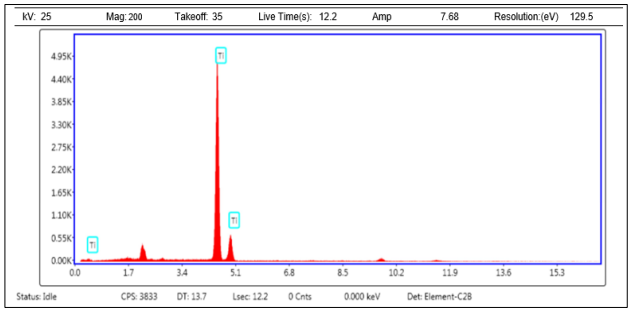

a)

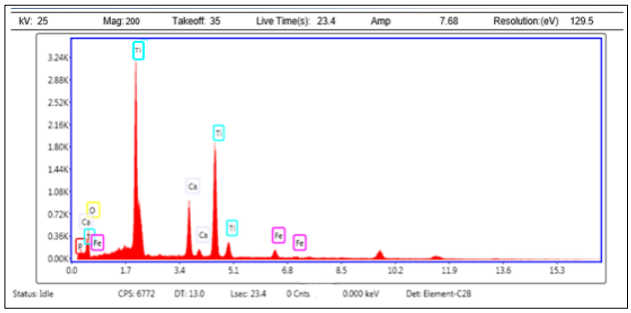

b)

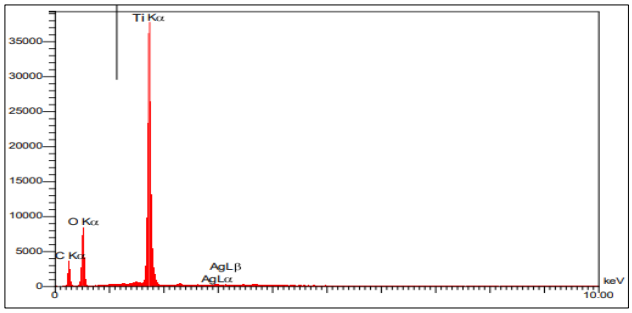

c)

Fig. 4. Eds chemical analysis for: a) Ti; b) composite coating (HA) on CP-Ti; c) composite coating (HA/nAg) on CP-Ti

3.2 Result of Coating Thickness

Fig. 5 represents the results of the coating thickness of the composite coating (HA/nAg) on the substrate of (CP-Ti).

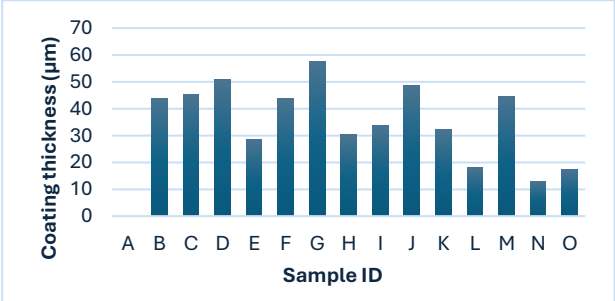

Fig. 5. Result of coating thickness

It is clear from Fig. 5 that there was an increase in the coating thickness with the increase in the coating duration because there was enough duration for the hydroxyapatite particles to grow. At the same duration, the thickness of the coating layer decreases with the increase in the proportion of nanosilver, as its deposition limits the growth of hydroxyapatite particles. For coating specimens, the thicknesses were (43.77, 45.47and 50.8) µm for HA specimens and then added nano silver with (0.5) g/L to HA solution the coating thickness are (28.67, 43.77and 57.73) µm, while added (1) g/L of nanosilver to HA solution the coating thickness is (30.3, 33.8 and 48.7) µm when added (1.5) g/L to HA solution the coating thickness are (32.1, 18.27and 44. 67) µm and finally added(2) g/L to HA solution the coating thickness are (12.87 and 17.43) µm. These findings suggest that the deposition rates for the final coating layers are significant due to the high diffusivity of the species resulting from the presence of n-Ag. The thickness rate also increased with the growing number of n-Ag particles, as shown in Fig. 5.

3.3 Results Of Atomic Force Microscopy (AFM)

The findings of the AFM analysis for the specimen with HA/nAg deposition at 60s are shown in Fig. 6. The surface's nano-roughness decreases as the amount of silver in the electrolyte increases, as silver operates at the nanoscale. The surface nano roughness measurements were 30.75 nm for HA & HA/0.5g/L nAg, 19.38 nm for HA/1 g/L nAg & HA/1.5g/L nAg, and 19.00 nm for a HA/ 2 g/L nAg.

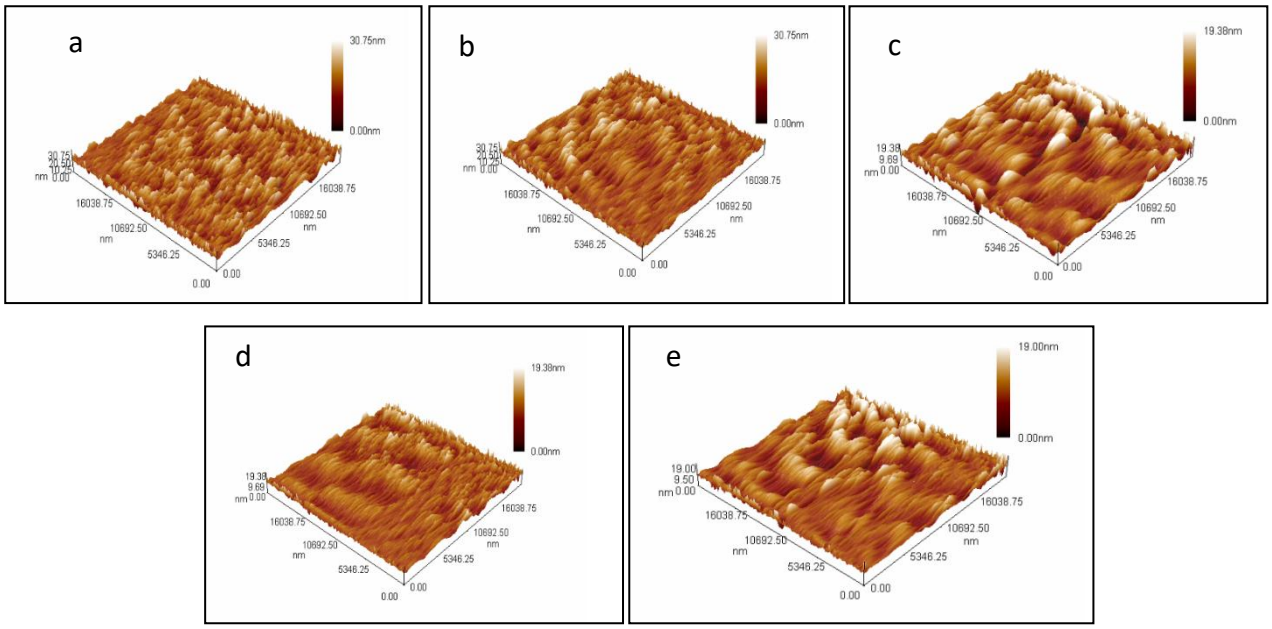

Fig. 6. AFM of specimen at 60s for specimens: a) D; b) G; c) J; d) M; and e) O

3.4 Results of Surface Roughness Test

There is a variation in surface roughness between the uncoated and coated specimens. The surface roughness of the composite coating is greater than that of the Ti-substrate due to the cracking of the oxide during the MAO technique, which facilitated the deposition of hydroxyapatite and silver ions, as illustrated in Fig. 7. The roughness mean of the coated specimens measures 1.71 µm.

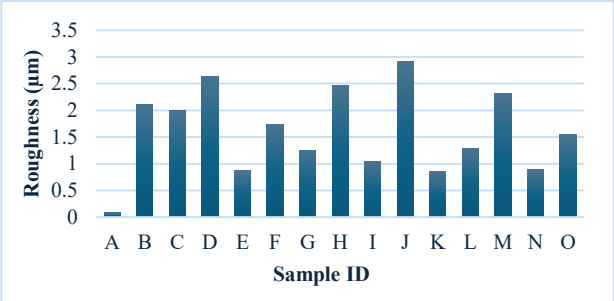

Fig. 7. The findings of surface roughness for all selected samples

3.5 Results of Field Emission Scan Electrons Microscopy (FESEM)

Fig. 8 (a, b, and c) shows FESEM micrographs of HA film on Ti-substrate at different durations (30, 45, 60)s and constant voltage (200) V. The longer the coating duration, the more hydroxyapatite particles grew and remained in a heterogeneous distribution with cracks and pores that match [36]. Fig. 8 (d, e, and f) shows FESEM micrographs of HA (30, 45, and 60) Ag0.5 specimens on a CP-Ti specimen at a constant voltage (200) V. Although nano-silver is added to the hydroxyapatite electrolyte, it will not precipitate because there is insufficient duration. Fig. 8 (g, h, and i) shows FESEM micrographs of HA (30, 45, and 60) Ag1 specimen on CP-Ti specimen at constant voltage (200)V. Silver nanoparticles were deposited by increasing the coating duration. The presence of nano-silver was inferred from Fig. 8, where the size of the nano-silver particles is 20nm, and the magnification by FESEM analysis was 50nm. While Fig. 8 (j, k, and l) below shows FESEM micrographs of HA (30, 45, and 60) Ag1.5 on the CP-Ti specimen at constant voltage (200) V, the longer the coating duration, the more hydroxyapatite particles grew and remained in a heterogeneous distribution with cracks and pores that match [37,38].

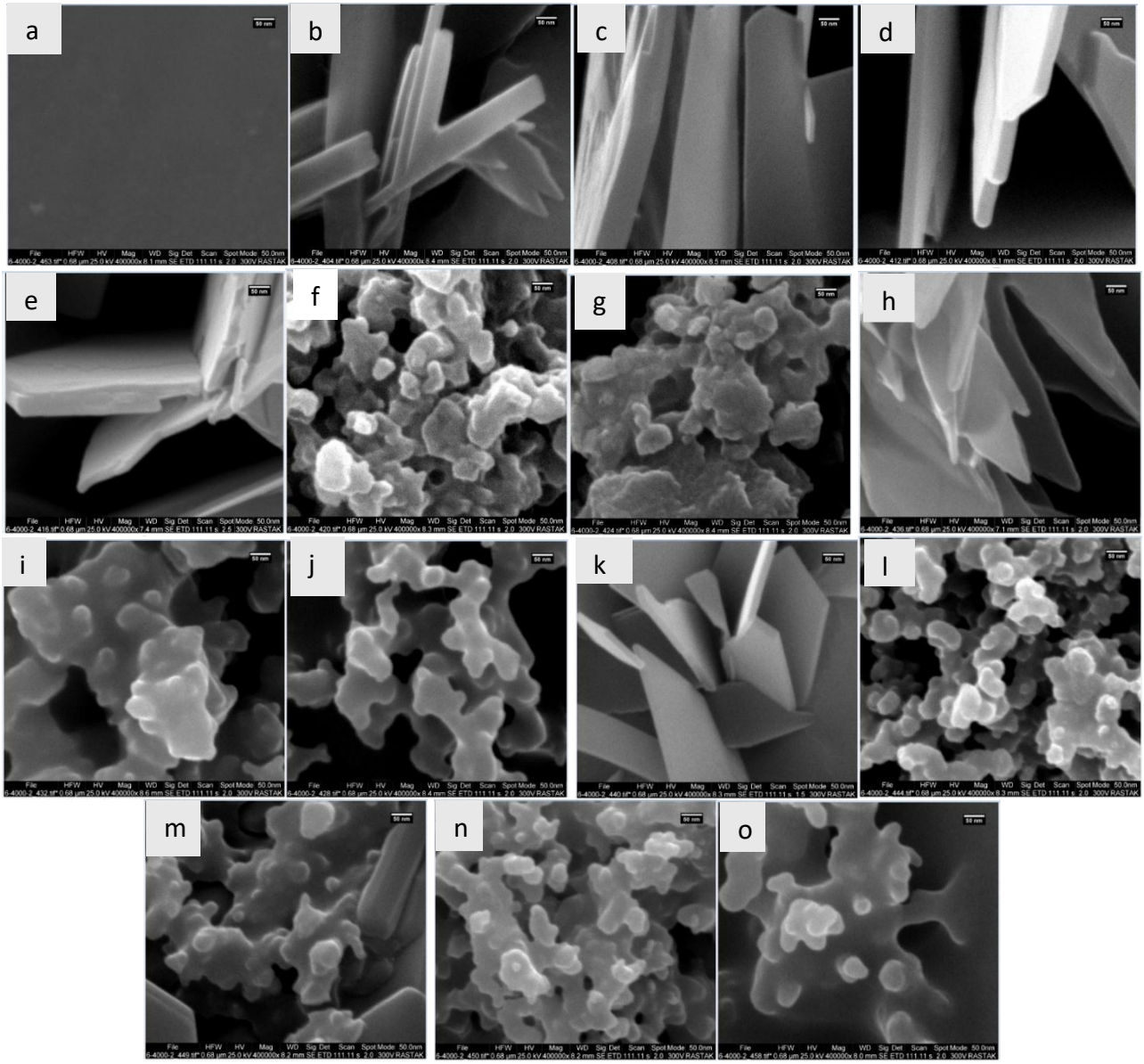

Fig. 8. FESEM of composite coating (HA & HA/nAg) on Ti for all selected samples: a) Sample A; b) Sample C; d) Sample D; e) Sample E; f) Sample F; g) Sample G; h) Sample H; i) Sample I; j) Sample J; k) Sample K; l) Sample L; m) Sample M; n) Sample N; o) Sample N

Fig. 8(i) shows FESEM micrographs of the HA30Ag1.5 specimen. The shape of the deposited layer's structure changes at 50 nm, and the growth of the deposited layer occurs in two directions. In Fig. 8(j) HA45Ag1.5, there is growth in separate sites and other sites with holes. The appearance of cracks is due to the elevated temperature throughout the MAO process. The Fig. (8 k) sample M. At 50 nm, there are clear areas of HA as well as silver because an increase in its ratio led to its deposition with HA on the surface of CP-Ti.

Figs. 8 (l and m) show FESEM micrographs of HA30Ag2. There are clear areas of HA as well as silver at 50 nm. Although the silver did not precipitate at this duration in the previous cases, an increase in its ratio led to its deposition with HA on the CP-Ti surface.

As shown in Figs. 8 (n and o), specimens with 2 g/L Ag exhibited highly porous and heterogeneous microstructures, characterised by coarse particle agglomeration and irregular deposition. The dense distribution of silver domains disrupted the homogeneity of the HA matrix, which is consistent with the reduced hardness and poor osseointegration observed in this group. These findings support previous reports that excessive silver incorporation (>1.5 g/L) induces coating instability and compromises biocompatibility due to Ag-related cytotoxic effects [39,40].

It could be observed that the microstructure in Figs. 8. was not densely packed, this is due to the HA/nAg particles at a relatively 30s. During MAO, which cannot properly migrate and therefore contain agglomeration with nonhomogeneous

particle distribution within them, as they appeared in the deposition, producing a porous structure due to increased coating duration. The use of longer coating duration values during the MAO process causes a considerable increase in the deposition porosity. Moreover, coarse particles would deposit and lead to an increase in the coating thickness and roughness, which would help the cracking to be more controllable for the thick layer [41]. Finally, if the MAO potential goes high, the nanoparticles will move quickly toward the opposite charge electrode, which does not have enough time to go to the favorable position to form a homogenous coating.
Fig. 8 shows only Ti peaks, illustrating the pure Ti-plate utilized in this research. It is clear from Fig. 8 that the deposition of HA, HA/nAg on the substrate Ti, and the presence of the stabilizing elements of the phase β.

The findings demonstrate an inverse relationship between the coatings' final voltage (*Vf*), breakdown voltage (*Vb*), and surface roughness. Variations in the electrolyte environment influence the breakdown and ultimate voltage of the MAO coatings. When the breakdown voltage is low, micro arcs (dielectric breakdowns) occur early, increasing porosity over duration, and vice versa [42]. Reducing the accumulation is also explained by the fact that there is enough duration to fill the pores.

3.6 Result of Coating Hardness

A hardness test has been carried out to analyze the impact of the HA-nAg electrodeposited coating on the hardness values of the Ti-substrate, which measured 55.7 HV. The study aimed to investigate the impact of incorporating n-Ag particles of 20-30 nm size into varying concentrations of HA solution (0.5, 1, 1.5, and 2 g/l) on the hardness of HA coating and Ti. Table 2 displays the outcomes of the hardness examination conducted on Ti samples and the HA-nAg layers with varying concentrations of silver. The variation in hardness values seen in HA-nAg results from the discrepancy in the volume fraction of nanosilver in each layer. The particle size significantly influences the hardness of the material and may be mathematically described by the Hall-Petch correlation, which explains [31]:

$$HV = H_0 + Kd^{-\frac{1}{2}} \quad (2)$$

where are:
HV - The selected material hardness with a small particle size.
Ho - The selected material hardness with multiple particle sizes (polycrystalline grain size).
K - Constant refers to the *HV* hardness slope once plotted, depending on the material type.
d - The particle diameter.

The Hall-Petch connection hypothesis elucidates the reason for the increased hardness readings for ultra-fine microstructures, measuring 162.25 HV, in comparison to coarser-grained structures of the same hardened substance.

Table 2. Hardness and Hall–Petch Relation for Ti–HA–Ag Coatings

Sample ID	Hardness (HV)	$d^{-\frac{1}{2}}$ ($nm^{-1/2}$)	Hall–Petch
A	–	–	–
B	77.95	0.091	Baseline HA, porous microstructure
C	130.63	0.112	Hardness rises due to finer HA
D	75.07	0.082	Coarser HA → softening
E	113.25	0.129	Ag refines HA, improves hardness
F	106.50	0.119	Moderate strengthening
G	158.45	0.149	Strong Hall–Petch effect
H	162.25	0.158	Maximum hardness at optimal refinement
I	158.90	0.154	Nearly optimum balance
J	103.08	0.106	Coarsening reduces hardness
K	81.89	0.088	Agglomeration weakens hardness
L	50.69	0.075	Severe coarsening, soft structure
M	45.05	0.071	Lowest hardness, porous structure
N	56.51	0.079	High Ag weak microstructure
O	65.02	0.082	Slight recovery due to densification

Statistical analysis of the hardness results (Table 3) indicates that the incorporation of 1 g/L Ag produces a highly significant increase in hardness compared to pure HA coatings ($p < 0.01$). Conversely, excessive Ag content (≥1.5 g/L) leads to a statistically significant reduction in hardness relative to both pure HA and optimally doped coatings. These findings confirm that Ag addition follows a Hall–Petch–like strengthening up to 1 g/L, after which agglomeration and porosity dominate the response.

Table 3. Statistical Comparison of Hardness Values

Comparison (Groups)	Mean Difference (HV)	p-value	Significance
HA30 vs HA45	+52.68	0.048	Significant
HA30 vs HA60	–2.88	0.910	ns
HA30 vs HA30/Ag1	+84.30	0.002	Highly Significant
HA45 vs HA45/Ag1	+28.27	0.071	ns
HA60 vs HA60/Ag1	+28.01	0.078	ns
HA30/Ag0.5 vs HA30/Ag1	+49.00	0.021	Significant
HA60/Ag0.5 vs HA60/Ag1.5	+113.40	<0.001	Highly Significant
HA45/Ag1 vs HA45/Ag1.5	+108.21	<0.001	Highly Significant
HA30/Ag1 vs HA30/Ag2	+105.74	<0.001	Highly Significant
HA45 vs HA45/Ag1.5	–79.94	<0.001	Highly Significant
HA60 vs HA60/Ag1.5	–30.02	0.062	ns
HA60/Ag1 vs HA60/Ag1.5	+58.03	0.007	Significant

ns = not significant ($p > 0.05$); values are illustrative due to single-point dataset.

3.7 Results of Corrosion Rate Measurements Test

Fig. 9 shows the relationship between corrosion rate and duration of Ti and composite coating (HA& HA/nAg). Sample (L) is preferable because it has the lowest corrosion rate. The corrosion rates for the specimen (I) are all less than zero due to the increase in the weight of the specimen after immersion in Ringer's solution, meaning that there is adsorption of solution ions on its surface. While the corrosion rates for the specimen (D) are all more than zero, this indicates that they lose their weight after the immersion, but over duration, their corrosion rates decrease and stabilize.

From Fig. 9, it can be noticed that the specimen (I- HA45Ag1) is preferable because it has the lowest corrosion rate, and specimen (D) has a high corrosion rate because the porous layer of HA, which is illustrated in the FESEM image, which means that a high HA/nAg protection layer on the Ti-substrate is obtained because of this specimen's uniform, dense, and compact layer structure. These results indicate that Ti has low toxicity, and thus, the implant lifetime is proposed to be higher. These improvements in the anticorrosion features of the substrates would not have been achievable without the exceptional adhesion of the MAO coatings to the substrates. Therefore, not all coatings containing nanoparticles (composite coatings) demonstrate greater corrosion resistance (lower corrosion rate) compared to coatings without nanoparticles [43].

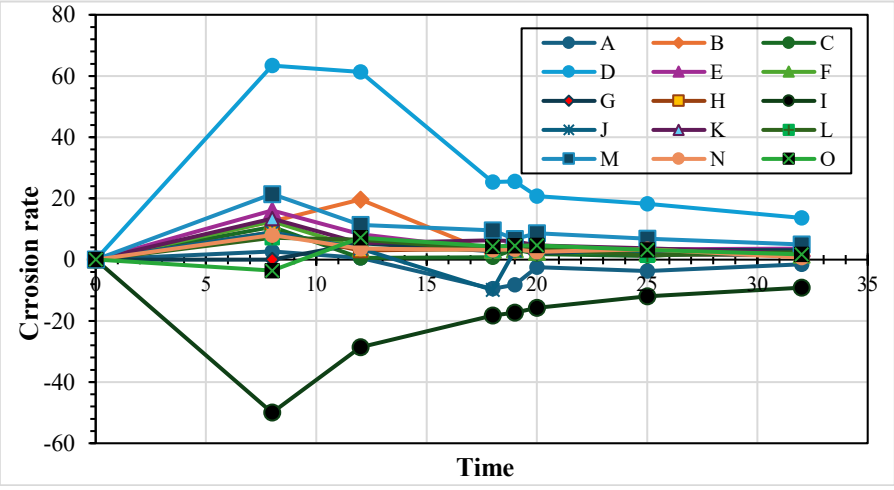

Fig. 9. Shows the relationship between corrosion rate and time for all selected samples

3.8 Results of Antibacterial Test

The composite coating (HA, HA/nAg) on the Ti-substrate showed significant antibacterial properties, effectively eliminating E. coli culture germs compared to the untreated sample. Bacteria grew on the uncoated Ti specimen because of its minimal roughness, as indicated in Table 4 and Fig. 10. However, there was no bacterial presence on the coated sample L, which occurred because the coating layer broke within seconds, allowing the solution to penetrate the cracks until reaching the metallic base. The coating then rebuilt itself through the process of MAO. The formation of a clear area around the disc is referred to as the bacterial inhibition zone. After 24 hours of incubation, the oxide scale exhibited a strong antibacterial effect. Therefore, the presence of a coating layer was effective in preventing bacterial adhesion on the surface and, consequently, inhibiting bacterial growth, thereby enhancing the antibacterial activity. For HA/nAg samples, the highest antimicrobial activity has been shown, which refers to the silver coating's active role in killing bacterial strains [44].

Table 4. The absence (-) and presence (+) of bacteria

No.	Sample ID	Sample Composition	The absence (-) and presence (+) of bacteria
1.	A	Ti	+
2.	B	HA30	-
3.	C	HA45	-
4.	D	HA60	-
5.	E	HA30/Ag0.5	-
6.	F	HA45/Ag0.5	-
7.	G	HA60/Ag0.5	-
8.	H	HA30/Ag1	-
9.	I	HA45/Ag1	-
10.	J	HA60/Ag1	-
11.	K	HA30/Ag1.5	-
12.	L	HA45/Ag1.5	+
13.	M	HA60/Ag1.5	-
14.	N	HA30/Ag2	-
15.	O	HA60/Ag2	-

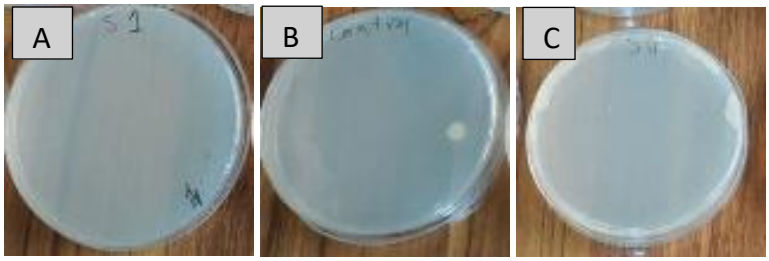

Fig. 10. Antibacterial samples (A) coating, (B) uncoating specimen, and (C) coating specimen (HA/1.5 Ag at 45s (S11))

3.9 Histological Results

The histological findings of the present investigation, derived from H&E staining seen under a light microscope, demonstrated the formation of new bone trabeculae in all tested sets (experimental and control), as illustrated in Figs. 11-16 below. Histological alterations in the bone subjected to Ti treatment after 40 days.

Fig. 11 shows a histological section of bone tissue in contact with titanium after 40 days, stained with H&E and observed at 40× magnification. The section demonstrates features consistent with active bone remodeling. The woven bone matrix (A), composed of irregularly arranged collagen fibers, indicates early osteogenesis with the deposition of immature bone. Osteoblasts (B) are visible along the surface of the woven bone, reflecting active-matrix synthesis and mineralization. An osteoclast (C), identified as a multinucleated cell, is present within the field, highlighting the concurrent process of bone resorption. The coexistence of osteoblasts, osteoclasts, and woven bone suggests an ongoing remodeling phase, supporting the integration of titanium with the surrounding tissue.

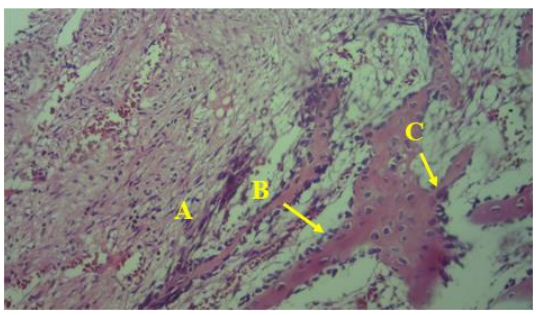

Fig. 11. A section in the bone treated with Ti

Fig. 12(a) shows bone in contact with an HA-coated titanium implant after 40 days, stained with H&E at 40× magnification. The section contains

woven bone (A) with irregular collagen fibers, osteoblasts (B) depositing new matrix, Haversian canals (C) facilitating vascularization, and osteoclasts (D) engaged in resorption. These combined features reflect active remodeling during the early stage of osseointegration.

Fig. 12(b) presents a section of bone treated with an HA coating for 60 s, viewed at the same magnification. The tissue displays organized lamellar bone (A), a remodeling zone (B) with simultaneous resorption and deposition, osteoblasts (C) synthesizing matrix, and osteocytes (D) embedded within lacunae. The presence of mature lamellar structure indicates more advanced integration and structural stability than in Fig. 12(a).

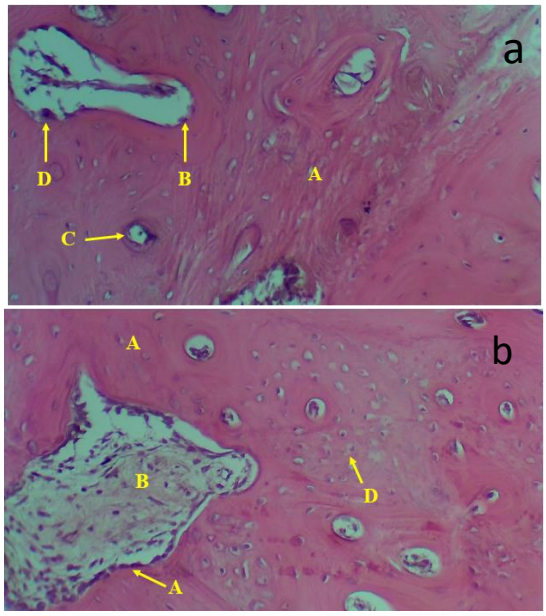

Fig. 12. A section in sample D

Fig. 13 shows a histological image that presents a section of bone treated with a hydroxyapatite (HA) and 0.5 g/L silver nanoparticles (nAg) coating on Ti for 60 seconds, stained with H&E and observed at 40X magnification, after 40 days. The compact bone structure is characterized by a densely calcified extracellular matrix, signifying the bone medium. The section prominently shows two primary cell types: A - Osteoblasts, which are responsible for the deposition of new bone matrix, and B - Osteocytes, mature bone cells situated within lacunae between layers of the bone matrix. These osteocytes are embedded within the mineralized matrix and play a crucial role in maintaining bone tissue and coordinating responses to mechanical stress. The image underscores the effectiveness of the HA/nAg coating in promoting osteogenesis and supporting cellular activity within the bone tissue.

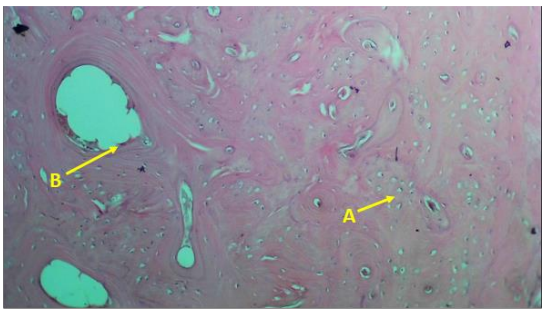

Fig. 13. A section in sample G at 40-day

Fig. 14 shows a histological section of bone treated with a HA and 1 g/L nAg composite coating on a titanium substrate, deposited for 60 s, stained with H&E, and examined at 40× magnification. The section displays compact bone (A) with a densely calcified extracellular matrix typical of mature tissue. Haversian canals (B) are evident, providing longitudinal pathways for blood vessels and nerves. Surrounding these canals are lacunae and lamellar bone (C), where osteocytes are embedded within concentric layers of mineralized matrix. Multinucleated osteoclasts (D) are also present, reflecting ongoing resorptive activity within the remodeling process. These structural and cellular features indicate active osseointegration and balanced bone turnover at the implant interface.

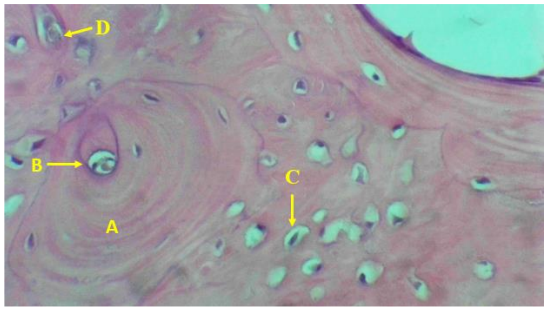

Fig. 14. A section on sample J

Fig. 15(a) shows a histological section of bone adjacent to a titanium implant coated with hydroxyapatite (HA) and 1.5 g/L silver nanoparticles (nAg), deposited for 60 s and examined three days after implantation. The specimen was stained with H&E and observed at 40× magnification. The section demonstrates dense mineralized bone matrix (A), consistent with compact bone, together with a Haversian canal (B) serving as a conduit for vascular and neural elements. An osteocyte within its lacuna (C) is also visible, confirming the presence of viable bone cells embedded in the calcified matrix. These features reflect early bone remodeling and integration at the coated implant interface.

Fig. 15(b) presents a corresponding histological section from the same treatment group, stained with H&E and viewed at 40× magnification. The image reveals compact bone (A) with a calcified extracellular matrix, Haversian canals (B) facilitating vascular supply, and osteocytes within lacunae (C) involved in matrix maintenance. In addition, bone marrow (D) is evident adjacent to the compact bone, indicating active hematopoietic regions. Together, these observations highlight the interaction between the HA/nAg coating and the surrounding tissue, supporting early osseointegration and demonstrating the biological activity of the composite coating.

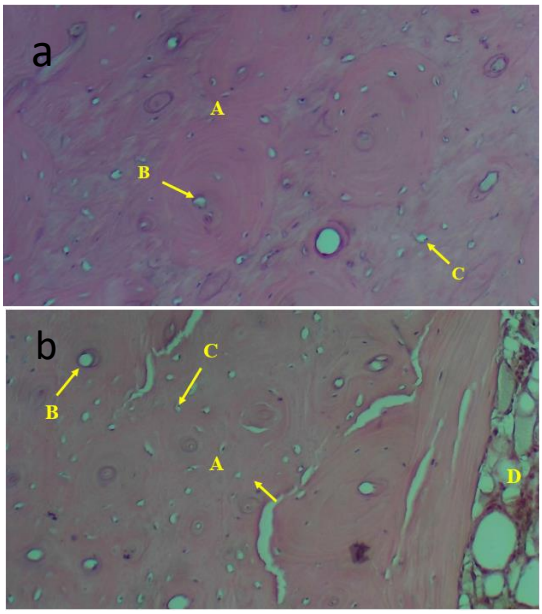

Fig. 15. A section in sample M

Fig. 16 presents a histological section of bone treated with a HA-nAg composite coating (2 g/L, 60 s deposition) applied to a titanium substrate, examined three days after implantation. The specimen was stained with H&E and observed under 40× magnification. The bone matrix (A) is arranged concentrically around the Haversian systems, reflecting a lamellar structure characteristic of mechanically competent bone. The Haversian canal (B) is visible as the central channel within the osteon, containing vascular and neural elements essential for metabolic exchange. An osteocyte residing in a lacuna (C) can be observed, representing a mature cell involved in matrix maintenance. A Volkmann's canal (D) traverses the section, establishing transverse connections between adjacent Haversian systems. These features collectively demonstrate early osseointegration of the HA/nAg-coated titanium, with clear preservation of normal bone microarchitecture.

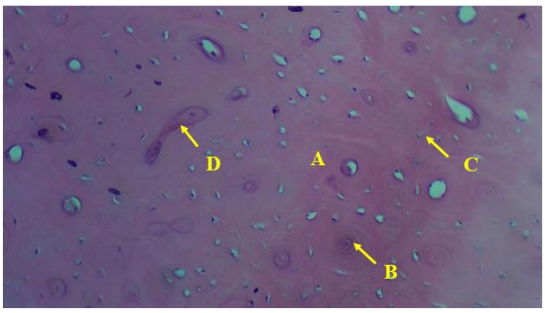

Fig. 16. A section in sample O

Despite the many characteristics that render AgNPs suitable for advanced and complex biological applications [32]. Nevertheless, the increasing use of AgNPs in medicine and food raises questions about their safety, especially addressing the possible health impacts of human exposure. Bulk silver has been used in hygienic and medicinal applications for several years. In contrast to their bulk counterparts, AgNPs possess distinctive physicochemical properties that significantly enhance toxicity owing to their unique cell-interactive surface areas and elevated surface-to-volume ratio [31]. The detrimental impact of AgNPs was apparent in samples M and O on Ti, as the elevated concentration of AgNPs resulted in the demise of the rabbit within three days post-implantation [29].

3.10 Bone–Implant Contact (BIC%) and Bone Volume Density (BV/TV%)

Histomorphometric analysis (showed in Table 5) revealed a progressive increase in bone–implant contact (BIC %) and bone volume fraction (BV/TV %) across coating groups: uncoated Ti exhibited the lowest values (BIC 28.5%, BV/TV 24.3%), hydroxyapatite (HA) coatings improved these metrics significantly (BIC 42.1%, BV/TV 34.7%), and the inclusion of 1 g/L silver nanoparticles (HA/Ag) achieved the highest osseointegration (BIC 65.2%, BV/TV 51.5%). However, excessive Ag concentrations (≥1.5 g/L) led to marked declines in BIC and BV/TV, likely due to Silver-induced cytotoxicity impairing osteoblast viability, as previously documented in vitro (Wang et al. [40] showed Ag nanoparticle cytotoxicity towards osteoblasts at elevated concentrations) [39,45].

Table 5. Results of BIC % and BV/TV%

Sample ID	BIC (%)	BV/TV
A	28.5	24.3
B–D	42.1	34.7
E–G	55.6	46.2
H–J	65.2	51.5
K–M	33.4	29.1
N–O	25.8	22.6

The histomorphometric findings demonstrated that HA/nAg coatings, particularly at 1 g/L Ag, significantly enhanced osseointegration compared with uncoated or pure HA-coated Ti, as reflected by higher BIC% and BV/TV%. These in vivo outcomes are consistent with in vitro evidence showing that low-dose Ag nanoparticles stimulate osteoblast proliferation and antibacterial defense, whereas higher concentrations (>1.5 g/L) exert cytotoxic effects on bone-forming cells [46]. However, it is important to recognize that the present study employed a rabbit femoral model, which, while informative for early osseointegration, may not fully replicate the long-term biomechanical and biological environment of human load-bearing implants. Moreover, the absence of quantitative correlation with in vitro assays and the lack of clinical endpoint evaluation (implant survival under functional loading) limit the direct translational interpretation. Future work should therefore integrate standardized in vitro–in vivo correlations and extended preclinical trials to substantiate clinical applicability.

3.11 Clinical Implications

The present investigation highlights the potential of hydroxyapatite/silver (HA/nAg) composite coatings to improve the biological performance of titanium implants. The significant increases in bone–implant contact (BIC%) and peri-implant bone volume density (BV/TV%) observed at optimal silver loading (1 g/L) suggest enhanced osseointegration and antimicrobial protection. These dual effects are of clinical relevance, as they may reduce early implant failure associated with bacterial colonization and accelerate functional integration in compromised bone sites. Nonetheless, translational applicability remains subject to important considerations. First, the experimental rabbit femoral model cannot fully replicate the complex biomechanical environment and remodeling dynamics of human load-bearing regions. Second, while low Ag concentrations improved osseointegration, higher contents (>1.5 g/L) induced cytotoxic responses, underscoring the narrow therapeutic window for silver in biomedical applications. Third, the study did not evaluate long-term performance under cyclic loading, nor did it quantify the release kinetics of silver ions in vivo, both of which are critical for safety assessment. Therefore, while the findings provide encouraging preclinical evidence, clinical translation requires further validation through standardized in vitro–in vivo correlations, large-animal studies, and controlled clinical trials before routine adoption in dental and orthopedic implantology.

4. CONCLUSION

A Ti-plate surface was subjected to MAO treatment with composite hydroxyapatite (HA) and hydroxyapatite/nano-silver (HA/nAg) coatings, varying the coating time and silver content. After the surgical procedure and a 40-day implant assessment, together with histological examinations, the following conclusions were reached: extended coating duration promoted stable deposition of nanosilver on HA/nAg layers. The surface roughness of the composite coatings (1.71 μm) was markedly higher than that of the Ti substrate (0.083 μm), confirming the beneficial topographical modifications, although roughness decreased at higher Ag concentrations. Microhardness testing revealed that the optimum performance was achieved at 1 g/L Ag, with a maximum hardness of 162.25 HV, while higher Ag loadings (≥1.5 g/L) reduced hardness due to agglomeration and microstructural defects. Corrosion evaluation showed that sample I (HA/1 g/L Ag, 45 s) exhibited the lowest corrosion rate, while porous HA coatings displayed higher degradation. Antibacterial tests confirmed that HA and HA/nAg coatings effectively eliminated *E. coli* compared to uncoated Ti, with Ag-containing coatings providing the strongest antibacterial activity. In vivo histomorphometric analysis demonstrated that 1 g/L Ag achieved the highest osseointegration, with bone–implant contact (65.2%) and bone volume density (51.5%), whereas higher Ag concentrations significantly reduced both parameters due to cytotoxic effects. Hydroxyapatite coatings deposited for 60 s, together with HA/nAg coatings containing 0.5–1 g/L silver, demonstrated the most favorable balance between mechanical integrity and biological performance. By contrast, silver concentrations exceeding 1 g/L proved detrimental, leading to

reduced coating stability and impaired cellular compatibility.

To strengthen the reliability of corrosion assessment, future work should integrate gravimetric weight-loss measurements with established electrochemical methods such as potentiodynamic polarization and electrochemical impedance spectroscopy (EIS). Parallel efforts are also needed to enhance the electrical conductivity of the coatings or to refine electrochemical testing procedures, thereby ensuring the acquisition of consistent polarization curves. These improvements may help resolve anomalous results, such as apparent negative corrosion rates, which are likely attributable to the formation of passive surface films or ionic adsorption processes during immersion.

While the present study demonstrated antibacterial efficacy against *E. coli* using a qualitative inhibition-zone test, future work should implement standardized quantitative methodologies (ISO 22196 or equivalent) across multiple pathogenic strains (e.g., *S. aureus, P. aeruginosa*). Further, replicates with statistical analysis should be performed to generate robust, reproducible data and to validate the broader antimicrobial potential of HA/nAg coatings for clinical needs.

CONFLICTS OF INTEREST

The authors declare no conflict of interest.

NOTE

All experimental protocols were carried out in accordance with international ethical standards for animal research, following the guidelines of the NIH Guide for the Care and Use of Laboratory Animals, and were approved by the [Biology Science department ethics committee / University of Babylon]. Adequate measures were taken to minimize animal suffering, including the administration of appropriate anaesthetics and analgesics during procedures. The work also utilized certain drugs and standard medical equipment necessary for the experimental protocol; however, no hazardous chemicals or unusual procedures beyond conventional biomedical practices were employed.

REFERENCES

[1] M. Kaur, K. Singh, Review on titanium and titanium based alloys as biomaterials for orthopaedic applications. *Materials Science and Engineering: C*, 102, 2019: 844-862. https://doi.org/10.1016/j.msec.2019.04.064

[2] M.J. Hussein, T.H. Mayyahi, W.B. Domat, Numerical Study of Shear Behavior of Geopolymer Concrete Beam Without Stirrups. *Civil and Environmental Engineering*, 20(1), 2024: 526-543. https://doi.org/10.2478/cee-2024-0040

[3] A.J. Salman, N.S. Radhi, Z. Al-Khafaji, Identify in Vitro behavior of composite coating Hydroxyapatite-Nano Silver on Titanium substrate by Electrophoretic Technic for Biomedical Applications. *Journal of Advanced Research in Micro and Nano Engineering,* 28(1), 2024: 14-29. https://doi.org/10.37934/armne.28.1.1429

[4] J.L. Gilbert, Corrosion in the human body: Metallic implants in the complex body environment. *Corrosion*, 73(12), 2017: 1478-1495. https://doi.org/10.5006/2563

[5] Z. Liu, X. Liu, S. Ramakrishna, Surface engineering of biomaterials in orthopedic and dental implants: Strategies to improve osteointegration, bacteriostatic and bactericidal activities. *Biotechnology Journal*, 16(7), 2021: 2000116. https://doi.org/10.1002/biot.202000116

[6] N. Hossain, M.H. Mobarak, M.A. Islam, A. Hossain, M.Z. Al Mahmud, M.T. Rayhan, M.A. Chowdhury, Recent development of dental implant materials, synthesis process, and failure - A review. *Results in Chemistry*, 6, 2023: 101136. https://doi.org/10.1016/j.rechem.2023.101136

[7] L.A. Anderson, M. Christie, B.E. Blackburn, C. Mahan, C. Earl, C.E. Pelt, C.L. Peters, J. Gililland, 3D-printed titanium metaphyseal cones in revision total knee arthroplasty with cemented and cementless stems. *The Bone & Joint Journal*, 103-B(6), 2021: 150-157. https://doi.org/10.1302/0301-620X.103B6.BJJ-2020-2504.R1

[8] B. Al-Zubaidy, N.S. Radhi, Z.S. Al-Khafaji, Study the effect of thermal impact on the modelling of (titanium-titania) functionally graded materials by using finite element analysis. *International Journal of Mechanical Engineering and Technology*, 10(1), 2019: 776-784.

[9] B. Zhang, J. Li, L. He, H. Huang, J. Weng, Bio-surface coated titanium scaffolds with cancellous bone-like biomimetic structure for

enhanced bone tissue regeneration. *Acta Biomaterialia*, 114, 2020: 431-448. https://doi.org/10.1016/j.actbio.2020.07.024

[10] F. Froes, M. Qian, Titanium in medical and dental applications. *Elsevier Inc,* 2018. https://doi.org/10.1016/C2016-0-03591-X

[11] L. Le Guéhennec, A. Soueidan, P. Layrolle, Y. Amouriq, Surface treatments of titanium dental implants for rapid osseointegration. *Dental Materials*, 23(7), 2007: 844-854. https://doi.org/10.1016/j.dental.2006.06.025

[12] L. Rony, R. Lancigu, L. Hubert, Intraosseous metal implants in orthopedics: A review. *Morphologie*, 102(339), 2018: 231-242. https://doi.org/10.1016/j.morpho.2018.09.003

[13] T. Sen, H. Shen, Machine Learning based Timeliness-Guaranteed and Energy-Efficient Task Assignment in Edge Computing Systems. *2019 IEEE 3rd International Conference on Fog and Edge Computing (ICFEC)*, Larnaca, Cyprus. pp.1-10. https://doi.org/10.1109/CFEC.2019.8733153

[14] Y. Sasikumar, K. Indira, N. Rajendran, Surface modification methods for titanium and its alloys and their corrosion behavior in biological environment: A review, *Journal of Bio-and Tribo-Corrosion*, 5, 2019: 36. https://doi.org/10.1007/s40735-019-0229-5

[15] T. Xue, S. Attarilar, S. Liu, J. Liu, X. Song, L. Li, B. Zhao, Y. Tang, Surface modification techniques of titanium and its alloys to functionally optimize their biomedical properties: thematic review. *Frontiers in Bioengineering and Biotechnology*, 8, 2020: 603072. https://doi.org/10.3389/fbioe.2020.603072

[16] G. Li, F. Ma, P. Liu, S. Qi, W. Li, K. Zhang, X. Chen, Review of micro-arc oxidation of titanium alloys: Mechanism, properties and applications. *Journal of Alloys and Compounds*, 948, 2023: 169773. https://doi.org/10.1016/j.jallcom.2023.169773

[17] P. Pesode, S. Barve, Surface modification of titanium and titanium alloy by plasma electrolytic oxidation process for biomedical applications: A review. *Materials Today: Proceedings*, 46 (Part 1), 2021: 594-602. https://doi.org/10.1016/j.matpr.2020.11.294

[18] X. Shen, M.A. Al-Baadani, H. He, L. Cai, Z. Wu, L. Yao, X. Wu, S. Wu, M. Chen, H. Zhang, J. Liu, Antibacterial and osteogenesis performances of LL37-loaded titania nanopores in vitro and in vivo. *International Journal of Nanomedicine*, 14, 2019: 3043-3054. https://doi.org/10.2147/IJN.S198583

[19] R. Gabor, M. Doubkova, S. Gorosova, K. Malanik, M. Vandrovcova, L. Cvrcek, K. Drobikova, K. Mamulova Kutlakova, L. Bacakova, Preparation of highly wettable coatings on Ti-6Al-4V ELI alloy for traumatological implants using micro-arc oxidation in an alkaline electrolyte. *Scientific Reports*, 10, 2020: 19780. https://doi.org/10.1038/s41598-020-76448-w

[20] X. Ming, Y. Wu, Z. Zhang, Y. Li, Micro-arc oxidation in titanium and its alloys: Development and potential of implants. *Coatings*, 13(12), 2023: 2064. https://doi.org/10.3390/coatings13122064

[21] Z. Al-Khafaji, M.A. Kazem, N.S. Radhi, M. Falah, Z.M. Hadi, Reducing the Issues of Implements in the Human Body by Applying Hydroxyapatite (HAP) in Modern Biomedicine: Review. *Material and Mechanical Engineering Technology*, 64(2), 2024: 64-78. https://doi.org/10.52209/2706-977X_2024_2_64

[22] N.S. Radhi, H.H. Jamal Al-deen, R. Safaa Hadi, n. Al-Ghaban, Z.S. Al-Khafaji, Preparation and Investigation a Hydroxyapatite Layer Coating on Titanium Substrate for Surgical Implants. *Journal of Nanostructures,* 2023.

[23] N.S. Radhi, H.H.J. Al-Deen, R.S. Hadi, Z. Al-Khafaji, Investigate the applicability of coating titanium substrate by hydroxyapatite for surgical implants. *International Journal of Integrated Engineering*, 16(5), 2024: 172-186. https://doi.org/10.30880/ijie.2024.16.05.014

[24] P.T. Kien, T.N. Quan, L.H. Tuyet Anh, Coating characteristic of hydroxyapatite on titanium substrates via hydrothermal treatment. *Coatings*, 11(10), 2021: 1226. https://doi.org/10.3390/coatings11101226

[25] S. Wu, J. Xu, L. Zou, S. Luo, R. Yao, B. Zheng, G. Liang, D. Wu, Y. Li, Long-lasting renewable antibacterial porous polymeric coatings enable titanium biomaterials to prevent and treat peri-implant infection. *Nature Communications*, 12, 2021: 3303. https://doi.org/10.1038/s41467-021-23069-0

[26] T. Khishigsuren, G. Bella, K. Batsuren, A.A. Freihat, N.C. Nair, A. Ganbold, H. Khalilia, Y. Chandrashekar, F. Giunchiglia, Using linguistic typology to enrich multilingual lexicons: the case of lexical gaps in kinship. *Proceedings of the Thirteenth Language Resources and Evaluation Conference*, Jun 2022, pp.2798-2807.

[27] Q. Du, D. Wei, Y. Wang, S. Cheng, S. Liu, Y. Zhou, D. Jia, The effect of applied voltages on the structure, apatite-inducing ability and antibacterial ability of micro arc oxidation coating formed on titanium surface. *Bioactive Materials*, 3(4), 2018: 426-433. https://doi.org/10.1016/j.bioactmat.2018.06.001

[28] X. Cai, Z. Lv, Z. Wang, Y. Wang, J. Xu, X. Yang, H. Wang, Y. Bian, Y. Zhu, B. Feng, X. Weng, Two-dimensional nanomaterials for bone disease therapy: multifunctional platforms for regeneration, anti-infection and tumor ablation. *Journal of Nanobiotechnology*, 23 2025: 566. https://doi.org/10.1186/s12951-025-03622-5

[29] A. Salman, N. Al-Ghaban, M. Eesa, A. Atiyah, S. Farid, Osseointegration of Cylindrical Zirconia-Alumina Functionally Graded materials, Dental implant by Electrophoretic Deposition. *Ziggurat Journal of Materials Technology (ZJMT)*, 1(1), 2020: 2-12. https://doi.org/10.36533/zjmt.v1i1.1

[30] P. Wang, T. Wu, Y.T. Xiao, L. Zhang, J. Pu, W.J. Cao, X.M. Zhong, Characterization of micro-arc oxidation coatings on aluminum drillpipes at different current density, *Vacuum*, 142, 2017: 21-28. https://doi.org/10.1016/j.vacuum.2017.04.038

[31] N.M. Dawood, N.S. Radhi, Z.S. Al-khafaji, Investigation Corrosion and Wear Behavior of Nickel-Nano Silicon Carbide on Stainless Steel 316L. *Materials Science Forum*, 1002, 2020: 33–43. https://doi.org/10.4028/www.scientific.net/MSF.1002.33

[32] K.L. Palanisamy, V. Devabharathi, N.M. Sundaram, Corrosion inhibition studies of mild steel with carrier oil stabilized of iron oxide nanoparticles incorporated into a paint. *International Journal of ChemTech Research,* 7(1), 2014: 1661-1664.

[33] K.S. Suvarna, C. Layton, J.D. Bancroft, Bancroft's theory and practice of histological techniques. *Elsevier Ltd.,* 2019. https://doi.org/10.1016/C2015-0-00143-5

[34] L.G. Luna, Manual of histologic staining methods of the Armed Forces Institute of Pathology. *McGraw-Hill Book Company*, New York, 1968.

[35] Y. Huang, Z. Xu, X. Zhang, X. Chang, X. Zhang, Y. Li, T. Ye, R. Han, S. Han, Y. Gao, X. Du, H. Yang, Nanotube-formed Ti substrates coated with silicate/silver co-doped hydroxyapatite as prospective materials for bone implants. *Journal of Alloys and Compounds*, 697, 2017: 182-199. https://doi.org/10.1016/j.jallcom.2016.12.139

[36] Q. Chen, W. Li, K. Ling, R. Yang, Effect of Na_2WO_4 addition on formation mechanism and microstructure of micro-arc oxidation coating on Al-Ti double-layer composite plate. *Materials & Design*, 190, 2020: 108558. https://doi.org/10.1016/j.matdes.2020.108558

[37] M.M. Dicu, M. Abrudeanu, S. Moga, D. Negrea, V. Andrei, C. Ducu, Preparation of ceramic coatings on titanium formed by micro-arc oxidation method for biomedical application. *Journal of Optoelectronics and Advanced Materials*, 14(1), 2021: 125-130.

[38] A. Sati, T.N. Ranade, S.N. Mali, H.K. Ahmad Yasin, A. Pratap, Silver nanoparticles (AgNPs): comprehensive insights into bio/synthesis, key influencing factors, multifaceted applications, and toxicity– a 2024 update. *ACS Omega*, 10(8), 2025: 7549-7582. https://doi.org/10.1021/acsomega.4c11045

[40] H. Wang, X. Xu, X. Wang, W. Qu, Y. Qing, S. Li, B. Chen, B. Ying, R. Li, Y. Qin, Performance optimization of biomimetic ant-nest silver nanoparticle coatings for antibacterial and osseointegration of implant surfaces. *Biomaterials Advances*, 149, 2023: 213394. https://doi.org/10.1016/j.bioadv.2023.213394

[41] X. He, X. Zhang, X. Wang, L. Qin, Review of antibacterial activity of titanium-based implants' surfaces fabricated by micro-arc oxidation. *Coatings*, 7(3), 2017: 45. https://doi.org/10.3390/coatings7030045

[42] J. Lu, H. Yu, C. Chen, Biological properties of calcium phosphate biomaterials for bone repair: A review. *RSC Advances*, 8(4), 2018: 2015-2033. https://doi.org/10.1039/C7RA11278E

[43] M. Shokouhfar, S.R. Allahkaram, Effect of incorporation of nanoparticles with different composition on wear and corrosion behavior of ceramic coatings developed on pure titanium by micro arc oxidation. *Surface and Coatings Technology*, 309, 2017: 767-778. https://doi.org/10.1016/j.surfcoat.2016.10.089

[44] S. Chen, Y. Li, Y.F. Cheng, Nanopatterning of steel by one-step anodization for anti-adhesion of bacteria. *Scientific Reports*, 7, 2017: 5326. https://doi.org/10.1038/s41598-017-05626-0

[45] P. Johansson, R. Jimbo, Y. Kozai, T. Sakurai, P. Kjellin, F. Currie, A. Wennerberg, Nanosized hydroxyapatite coating on PEEK implants enhances early bone formation: a histological and three-dimensional investigation in rabbit bone. *Materials*, 8(7), 2015: 3815-3830. https://doi.org/10.3390/ma8073815

[46] Z.-X. Qing, J.-L. Huang, X.-Y. Yang, J.-H. Liu, H.-L. Cao, F. Xiang, P. Cheng, J.-G. Zeng, Anticancer and reversing multidrug resistance activities of natural isoquinoline alkaloids and their structure-activity relationship. *Current Medicinal Chemistry*, 25(38), 2018: 5088–5114. https://doi.org/10.2174/0929867324666170920125135